Uniform 2 nm Gold Nanoparticles Supported on Iron Oxides as Active Catalysts for CO Oxidation Reaction: Structure-Activity Relationship

Yu Guo [a], Dong Gu [c], Zhao Jin [a], Pei-Pei Du [b], Rui Si [b,*], Jing Tao [d], Wen-Qian Xu [e], Yu-Ying Huang [b], Sanjaya Senanayake [e], Qi-Sheng Song [a], Chun-Jiang Jia[a,*], Ferdi Schüth [c]

[a]Key Laboratory for Colloid and Interface Chemistry, Key Laboratory of Special Aggregated Materials, School of Chemistry and Chemical Engineering, Shandong University, Jinan 250100, China

[b]Shanghai Synchrotron Radiation Facility, Shanghai Institute of Applied Physics, Chinese Academy of Sciences, Shanghai 201204, China

[c]Max-Planck Institut für Kohlenforschung, Kaiser-Wilhelm Platz 1, Mülheim an der Ruhr, D-45470, Germany

[d]Condensed Matter Physics and Materials Science Department, and [e]Chemistry Department, Brookhaven National Laboratory, Upton, New York 11973, United States

Abstract

Uniform Au nanoparticles (~ 2 nm) with narrow size-distribution (standard deviation: 0.5–0.6 nm) supported on both hydroxylated (Fe_OH) and dehydrated iron oxide (Fe_O) have been prepared by either deposition-precipitation (DP) or colloidal-deposition (CD). Different structural and textural characterizations were applied to the dried, calcined and used gold-iron oxide samples. The transmission electron microscopy (TEM) and high-resolution TEM (HRTEM) described the high homogeneity of supported Au nanoparticles. The ex-situ and in-situ X-ray absorption fine structure (XAFS) characterization monitored the electronic and short-range local structure of active gold species. The synchrotron-based in-situ X-ray diffraction (XRD), together with the corresponding temperature-programmed reduction by hydrogen (H_2-TPR), indicated the structural evolution on the iron-oxide supports correlating to their reducibility. An inverse order of catalytic activity between DP (Au/Fe_OH < Au/Fe_O) and CD (Au/Fe_OH > Au/Fe_O) has been observed. Effective gold-support interaction results in high activity for gold nanoparticles locally generated by sintering of dispersed Au atoms on the oxide support in the DP synthesis, while hydroxylated surface favors the reactivity of externally introduced Au nanoparticles on Fe_OH support for the CD approach. This work reveals why differences in the synthetic protocol translate to differences in the catalytic performance of Au/FeO_x catalysts with very similar structural characteristics in CO oxidation.

Keywords: Gold Catalyst, Iron Oxide, CO oxidation, In-Situ X-Ray Technique, Metal-Support Interaction

1. Introduction

Low-temperature CO oxidation over supported nanosized gold catalysts has been one of the most extensively studied systems in heterogeneous catalysis [1–3]. However, this simple reaction, catalyzed by nanostructured gold, is still very difficult to understand in depth. It is known that various factors, including the size of gold nanoparticles [1,4,5], the valence state of gold species (metallic Au^0 and ionic $Au^{\delta+}$) [6–8], the oxide support [9–14], and the metal-support interaction [15,16], can influence the catalytic performance of supported gold catalysts. However, previous findings are rather controversial with respect to the origin of high activity of gold catalysts, and the debate over the reaction mechanism of low-temperature CO oxidation has continued for more than two decades because of the ultra sensitivity and complexity of the oxide-supported gold system. One of the origins of this debate lies in the interrelationship of the different factors mentioned above, which are very difficult to separate from each other in gold catalysis.

Gold on iron-oxide (Au/FeO_x) is one of the highly active catalysts for CO oxidation, and also is a typical system for the study of the chemistry of gold on oxide supports [4,5,17]. Regarding the widely studied coprecipitated (CP) Au/FeO_x catalysts those have wide size-distribution of gold particles (from sub-nanometer to more than 20 nm) [4], it has been discovered that as-dried samples are much more active for CO oxidation than those after sintering, indicating the negative effect of calcination with respect to activity [4,17]. In fact, the calcination of gold-iron oxide catalysts usually results in simultaneous structural changes of both the gold and the oxide support, i.e., small gold clusters (< 1 nm) with dominant cationic component are transformed into purely metallic nanoparticles (> 1 nm); in addition, the phase of the support changes from hydroxylated ferrihydrite to dehydrated hematite [17]. For such a catalyst system, the accurate analysis of the origin of CO oxidation activity is a substantial

challenge due to the combination between various structural and textural effects. Therefore, the separate synthesis of gold nanoparticles with narrow size distribution and iron oxide supports with specific structure is crucial to rationally investigate the structure-activity relationship of Au/FeO_x catalyst.

Therefore, in this paper, we try to identify the support effect and the formation of gold nanostructure of Au/FeO_x catalysts for CO oxidation by using deposition-precipitation (DP) [18] or colloidal-deposition (CD) [13] syntheses for anchoring gold on hydroxylated (Fe_OH) or dehydrated iron oxide (Fe_O) supports (Scheme 1). Highly dispersed gold nanoparticles (~ 2 nm) with narrow size distribution (standard deviation: 0.5–0.6 nm) were obtained. The catalysts were studied by a combination of high-resolution transmission electron microscopy (HRTEM), ex-situ and in-situ X-ray absorption fine structure (XAFS), and in-situ X-ray diffraction (XRD) techniques. These unique samples allow us to distinguish the different factors (particle size, metal-support interaction, surface hydroxyl effect) governing the catalytic activity of gold-iron oxide catalyst. It is also demonstrated how important the formation pathways (locally generated or externally introduced) of gold particles are for the generation of active sites.

2. Experimental

2.1. Catalyst preparation

2.1.1 Preparation of iron oxide supports [7]

In a typical procedure, 0.25 mol L^{-1} Na_2CO_3 aqueous solution was added drop-wise to 200 mL of 0.1 mol·L^{-1} $Fe(NO_3)_3$ aqueous solution under stirring at 80 °C until pH = 8.2, and left stirring for another 1 h. The precipitate was collected by filtration and washed with deionized (DI) water at 80 °C.

This precipitate was dried at 120 °C in air for ca. 12 h to generate the hydrated iron oxide support (Fe_OH). The oxide support (Fe_O) was obtained via calcination of Fe_OH in air at 400 °C for 2 h.

2.1.2 Preparation of gold-iron oxide catalysts via colloidal deposition [13]

For colloidal deposition, poly(vinyl alcohol) (PVA, M_w 10,000 from Aldrich, 80% hydrolyzed) was used as the protecting agent. Typically, 0.675 mL of 0.5 wt.% PVA solution (Au:PVA = 1.5:1 in weight) and 2 mL of 0.0125 mol·L^{-1} $HAuCl_4$ solution were added into 50 mL of Millipore water (18.25 MΩ) at room temperature under vigorous stirring. After stirring for 10 min, a rapid injection of 1.30 mL of 0.1 mol·L^{-1} $NaBH_4$ aqueous solution led to formation of a dark orange-brown solution. 0.5 g Fe_OH or Fe_O was then added to the colloidal gold solution immediately under vigorous stirring, which was continued for 6 h until complete adsorption of the gold (1 wt.%), which was indicated by decoloration of the solution. The solids were collected by filtration and washing with Millipore water to remove dissolved impurities (Cl^-, e. g.). After drying at 60 °C in air overnight, CD_Au/Fe_OH and CD_Au/Fe_O were obtained. All the above steps were carried out in the absence of light by covering all containers with aluminum foil.

2.1.3 Preparation of gold-iron oxide catalysts via deposition precipitation

Typically, 0.5 g support powder (Fe_OH or Fe_O) was suspended in 23 mL Millipore water. 2 mL of 0.0125 mol·L^{-1} $HAuCl_4$ aqueous solution was then added to the solution under stirring at ca. 60 °C. After 30 min, 25 mL of aqueous solution containing 0.5 g of urea was quickly added into the stock solution. Thereafter, the solution temperature was increased to 80 °C and kept under vigorous stirring for 3 hours to allow decomposition of urea, which resulted in a gradual increase of the pH value from 4.0 to 8.6. The solution was aged at room temperature for another 20 h. The as-obtained solids were

collected by filtration and then washed with Millipore water at 60 °C. After drying at 60 °C in air overnight, DP_Au/Fe_OH and DP_Au/Fe_O were obtained.

2.2 Characterization

The gold loadings of catalysts were determined by inductively coupled plasma atomic emission spectroscopy (ICP-AES) on an IRIS Intrepid II XSP instrument (Thermo Electron Corporation).

Transmission electron microscopy (TEM), high-resolution TEM (HRTEM) and the related high angle annular dark field-scanning TEM (HAADF-STEM) were conducted on a Philips Tecnai F20 instrument at 200 kV and a field emission TEM (JEOL 2100F) machine equipped with a 2k × 2k CCD camera at 200 kV. All the tested samples were ground in a mortar alone rather than suspended in ethanol before deposition on an ultra-thin carbon film-coated copper grid.

Temperature-programmed reduction by hydrogen (H_2-TPR) was carried out in a Builder PCSA-1000 instrument (Beijing, China) equipped with a thermal conductivity detector (TCD) to detect H_2 consumption. The sieved catalysts (20–40 mesh, 30 mg) were heated (5 °C·min^{-1}) from room temperature to 400 °C in a 20%H_2/Ar (30 mL·min^{-1}) gas mixture. Before measurement, the fresh samples were pretreated in pure O_2 at 300 °C for 30 min.

X-ray absorption fine structure (XAFS): Au L-III absorption edge (E_0 = 11919 eV) XAFS spectra were collected ex-situ at BL14W1 beamline of the Shanghai Synchrotron Radiation Facility (SSRF) operated at 3.5 GeV under “top-up” mode with a current of 220 mA. The XAFS data were collected in fluorescence mode with a 32 element Ge Solid State Detector (SSD). The in-situ experiments were conducted at the X18B beamline of the National Synchrotron Light Source (NSLS) at Brookhaven National Laboratory (BNL), operated at 2.8 GeV under “decay” mode with currents of 160–300 mA.

The powder sample (~ 25 mg) was loaded into a Kapton tube (O.D. = 0.125 inch) which was attached to an in-situ flow cell. Two small resistance heating wires were installed above and below the tube, and the temperature was monitored with a 0.5 mm chromel-alumel thermocouple that was placed inside the tube near the sample. The in-situ CO oxidation reaction (1%CO/16%O_2/83%He, 20 mL·min^{-1}) was carried out under a "steady-state" mode at room temperature (~ 25 °C). Each XAFS spectrum (ca. 15 min collection) was taken under fluorescence mode with a 4 element Vortex Silicon Drift Detector (SDD). The energy was calibrated for each scan with the first inflection point of the Au L-III-edge in Au metal foil. The X-ray absorption near edge spectroscopy (XANES) and extended X-ray absorption fine structure (EXAFS) data have been analyzed using the Athena and Artemis programs.

X-ray diffraction (XRD): The ex-situ and in-situ XRD experiments were carried out on X7B beamline (λ = 0.3196 Å) of NSLS at BNL. The powder sample (~ 2 mg) was loaded into a quartz tube (I.D. = 0.9 mm, O.D. = 1.0 mm) which was attached to the same flow cell as in the XAFS measurements. One small resistance heating wire was installed right below the tube, and the temperature was monitored with a 0.5 mm chromel-alumel thermocouple that was placed inside the tube near the sample. The in-situ H_2-TPR tests (5%H_2/Ar, 5 mL·min–1) were carried out using a temperature ramp between 25 and 400 °C (5 °C·min^{-1}), and then kept at 400 °C for 20 min. The fresh catalysts were pretreated in 5%O_2/He at 300 °C for 30 min before in-situ measurements. Two-dimensional XRD patterns were collected with an image-plate detector (Perkin-Elmer), and the powder rings were integrated using the FIT2D code.

2.3 Catalytic test

CO oxidation activities of gold-iron oxide catalysts were measured in a plug flow reactor by use of 50 mg of sieved (20–40 mesh) catalyst in a gas mixture of 1 vol% CO, 20 vol% O_2, and 79 vol% N_2

(from AIR LIQUIDE, 99.997% purity), at a flow rate of 67 $mL \cdot min^{-1}$, corresponding to a space velocity of 80,000 $mL \cdot h^{-1} \cdot g_{cat}^{-1}$. Prior to the measurement, the catalysts were pretreated in air at 300 °C for 30 min for activation. After that, the reactor was cooled down to −50 °C under a flow of pure N_2 gas. The catalytic tests were carried out in the reactant atmosphere by ramping the catalyst temperature (5 $°C \cdot min^{-1}$) from −50 to 300 °C. The outlet gas compositions of CO and CO_2 were online monitored by a non-dispersive IR spectroscopy (ABB EL 3020). A typical "steady-state" experiment (30 °C) was conducted in the same gas-mixture at 30 °C for more than 10 h.

3. Results and Discussion

Inductively coupled plasma atomic emission spectroscopy (ICP-AES) results (Table 1) show that the experimental Au loading of all four catalysts are close to the target value of 1 wt.%. The XRD data (Figure 1) reveal that the Fe_OH supports in the catalysts are semi-amorphous (see pattern a/b), probably a mixture of several hydroxylated iron oxide phases, even after air-calcination at 300 °C. On the other hand, Fe_O obtained by thermal dehydration of Fe_OH, is present as well-defined hematite (α-Fe_2O_3, JCPDS card#: 2-919) in both DP (pattern c) and CD (pattern d) samples, indicating the complete dehydration and crystallization during 400 °C air-calcination. The TEM images (Figures 2 and 3) allow determination of the sizes of Fe_OH and Fe_O supports to ~5 and 10−30 nm, respectively. For the dried DP samples, no gold clusters/particles were found by HRTEM (Figures 2a and 2b). This suggests that the gold atoms are well dispersed on the surfaces of iron-based supports before air-calcination. On the other hand, for the dried CD catalysts, ~ 2 nm Au nanoparticles on Fe_OH and Fe_O surfaces were clearly observed in TEM (Figures 3a and 3b) due to features of the colloidal deposition preparation, i. e. well-crystallized small-size gold particles already formed before adding the iron-based supports.

In addition to the characterization by electron microscopy, we also carried out XAFS analysis to determine the coordination state of the gold species (Table 2 and Figure 4). The X-ray absorption near edge structure (XANES) spectra reveal the ionic nature of Au species [19] in the dried DP catalysts (Figures 4a and 4b), and the related extended XAFS (EXAFS) spectra (Figures 4c and 4d) show the presence of a pure Au-O shell in the dried DP_Au/Fe_OH and DP_Au/Fe_O samples, with distances of the first coordination sphere of ca. 2.0 Å and coordination numbers (CN) of 2.5–2.9 by EXAFS fittings (Table 2), which are consistent with a previous report on fully oxidized $Au^{\delta+}$ species in gold-ceria catalysts [20]. For the CD samples, according to the corresponding XANES (Figure 5a) and EXAFS (Figure 5b) results, gold species were in metallic form with the CN of 10−11 (Table 2), well consistent with the Au^0 nanoparticle nature.

Upon calcination, the well-dispersed atomic gold species in DP samples were transformed to uniform small (ca. 2 nm) nanoparticles, as seen in the HAADF-STEM images in Figures 2c and 2d (also refer to Table 1). The XANES spectra display distinct metallic gold (Au^0) features for calcined DP_Au/Fe_OH and DP_Au/Fe_O catalysts (Figures 4a and 4b), and the corresponding EXAFS fitting results confirm this, since only Au-Au contributions (2.84 Å, CN = 10, refer to Table 2, Figures 4c and 4d) are present, instead of the Au-O shell in the dried samples. The formation of gold nanoparticles after 300 °C air-calcination demonstrates the relatively weak interaction between Au atoms and the Fe_OH or Fe_O support in DP samples than the widely studied coprecipitated Au/FeO_x catalysts, i. e. almost no change in the gold nanostructure during oxidative calcination in air at 400 °C or less [21].

The catalytic performance of the Au/FeO_x catalysts was evaluated for low-temperature CO oxidation. The transient profiles in Figure 6a reveal the higher activity of Au on Fe_O, compared to Au on Fe_OH (T_{90} = 18 °C vs 63 °C) for the DP samples. In contrast, for CD synthesis, the_Au/Fe_OH was

superior to CD_Au/Fe_O (T_{90} = 24 °C vs 56 °C). At constant temperature of 30 °C (Figure 6b), the final CO conversions after 10 h on stream were around 38%, 70%, 80% and 40% for sample DP_Au/Fe_OH, DP_Au/Fe_O, CD_Au/Fe_OH and CD_Au/Fe_O, respectively. The reactivity of different gold catalysts thus follows the sequence: DP_Au/Fe_O ≈ CD_Au/Fe_OH > DP_Au/Fe_OH ≈ CD_Au/Fe_O. The activities of the DP_Au/Fe_O and CD_Au/Fe_OH catalysts described here are comparable to those of commonly coprecipitated gold-iron oxide catalysts with even higher gold loading of ~ 5 wt.% [7].

Gold sizes in the used DP catalysts were investigated by TEM/HRTEM. Figure ~~3~~ 2 shows that the particles sizes did not change and were around 2 nm before and after the CO oxidation reaction. The related XANES (Figures 4a and 4b) and EXAFS (Figures 4c and 4d) spectra give additional evidence on the metallic nature of the nanoparticles. Similar observations with respect to particles size hold for the CD catalysts: the TEM/HRTEM images of the CD catalysts confirm that gold particle sizes on both Fe_OH and Fe_O supports are constant at ca. 2 nm for dried, calcined and used samples (Figure 3). It reveals that in CD catalysts the interaction between gold and the iron oxide support does not have a significant influence. The major structure is isolated Au nanoparticles randomly dispersed on Fe_OH or Fe_O surface, which can be confirmed by the related XAFS results on dried samples (Table 2 and Figure 5) and very similar to the gold-silica system [22].

Therefore, CD_Au/Fe_OH and CD_Au/Fe_O can be regarded as reference catalysts for the analysis of the support effect, i. e. ~ 2 nm Au on hydroxylated (Fe_OH) and dehydrated (Fe_O). Very interestingly, an inverse order of catalytic activity can be clearly seen from the related experimental data between DP (Au/Fe_OH < Au/Fe_O) and CD (Au/Fe_OH > Au/Fe_O). Recently, it has been reported that the surface hydroxyl groups of the support can enhance the activity of supported gold catalyst for CO oxidation [23-27]. For CD-prepared catalysts, it seems that surface hydroxyl effect plays the

dominant role in determining the activity, so that hydroxylated Au/Fe_OH is much more active than Au/Fe_O. However, it has an inverse effect for DP-prepared catalyst. This suggests that other factors should be more significant than surface hydroxyl effect in controlling the reactivity of gold-iron oxide catalysts prepared by the DP method. Since the development of the gold particles follows a much more complex pathway in DP, this is not highly surprising.

First, we focused on the investigation of structural changes of the gold species. Figure 7 exhibits the in-situ XANES results on both DP_Au/Fe_OH and DP_Au/Fe_O. The corresponding fraction of oxidized/reduced gold was calculated by the linear combination method [28], and the CO conversion was monitored by mass spectroscopy simultaneously. Although the starting Au nanostructures were nearly the same (~ 2 nm metallic particles), the CO oxidation activity of gold on the oxide support was much higher than that on the hydroxylated support (CO conversion at the end of measurement: 58% vs. 10%), in good agreement with Figure 6b. However, the oxidation states of Au were dominantly metallic (Au^0) and the ionic ($Au^{\delta+}$) contributions were below 10% in both samples. Besides, the EXAFS fitting results (Table 2 and Figure 4) further prove the predominance of reduced gold nanoparticles in the calcined (before reaction) and used (after reaction) DP catalysts. This demonstrates that the oxidation state is not the dominant factor governing the activity of gold-iron oxide catalysts obtained via the DP route.

Another factor which could lead to different catalytic activities of the different DP catalysts could be the transformation of the isolated Au atoms or small clusters (Figures 2a and 2b) into Au particles (Figures 2c and 2d), which takes place during air-calcination. In order to reveal possible differences, hydrogen temperature-programmed reduction (H_2-TPR) was applied to investigate the interaction between metal (Au) and the supports of Fe_OH or Fe_O (Figure 8 and Table 3). Figure 8a displays the

results: for the pure iron-based support, the main reduction peaks are located between 300 and 400 °C, due to the reduction of α-Fe_2O_3 (hematite) $\rightarrow$ Fe_3O_4 (magnetite). The introduction of gold led to a decrease of this temperature to about 128 and 232 °C, indicating a pronounced Au-O-Fe interaction [27]. Figures 8b and 8c show the XRD patterns obtained under in-situ conditions similar to the TPR conditions. For DP_Au/Fe_OH, the starting amorphous hydrated iron oxide was reduced and started to crystallize to Fe_3O_4 at ca. 200 °C, and was further reduced to Fe metal above 368 °C (Figure 8b). For DP_Au/Fe_O, the transformation of the iron oxide from α-Fe_2O_3 $\rightarrow$ Fe_3O_4 occurs at temperatures above 200 °C, the final point of the experiment is metallic Fe and traces of Fe_3O_4 at 400 °C (Figure 8c).

For the DP_Au/Fe_O catalyst, there is an intense reduction peak centered at 232 °C. The H_2 consumption related to this reduction peak is 1444 $\mu mol \cdot g^{-1}$ which is very close to the theoretical value (1510 $\mu mol \cdot g^{-1}$, Table 3), indicating the full reduction of most of the α-Fe_2O_3 to Fe_3O_4. However, for the DP_Au/Fe_OH, a broad reduction peak centered at 128 °C with a low H_2 consumption value of 437 $\mu mol \cdot g^{-1}$ is observed. The theoretical value of H_2 consumption related to a full transformation of Fe_OH$\rightarrow$$Fe_3O_4$ is 1300 $\mu mol \cdot g^{-1}$, which is much higher than that of the reduction peak centered at 128 °C for DP_Au/Fe_OH. Therefore, only part of the Fe_OH was reduced to Fe_3O_4 at a temperature of 200 °C (the end of the broad peak), in agreement with the in situ XRD pattern at 200 °C which covers both Fe_3O_4 and some amorphous phases, as shown in Figure 8b. The TPR results confirm an more effective interaction [20,27] of gold species with iron oxide than with hydroxylated amorphous iron oxide, which explains why the gold on the dehydrated support (Fe_O) is significantly more active than gold on the hydroxylated support (Fe_OH). It also suggests that the presence of the hydroxylated support prevents the creation of active Au sites during the crystallization of both gold and the iron-oxide support.

On the other hand, for the CD catalysts, the 2 nm Au nanoparticles are already formed before calcination, and the overall interaction between gold and iron-oxide support is less effective than for the DP samples (refer to the lower reduction peak-area for CD_Au/Fe_O in Figure 9a). Based on the related in-situ XRD results, the phase transformations of iron-oxide support in CD samples (Figures 9b and 9c) were very similar to those synthesized by DP (Figures 8b and 8c). Here, hydroxylated surface is the dominant factor on tuning the Au dispersion/stabilization, and thus the hydroxylated catalyst (CD_Au/Fe_OH) was more active than the dehydrated sample (CD_Au/Fe_O). However, also the surface hydroxyl groups may have an effect, since this type of support brings the extra activity enhancement for the gold catalyst systems [23–27].

From the results described it can be concluded that the preparation method (DP or CD), respectively, the formation mechanism of the gold particle formation (locally generated or externally introduced) are crucial in determining the gold reactivity. Deposition-precipitation, or local generation, benefits from the dehydrated support (Fe_O) only, while colloidal-deposition is better suited for the hydroxylated support (Fe_OH). For the DP route, the gold particles and their interaction with the support develop during thermal treatment. Here it is clear that the more strongly interacting gold species lead to more active catalysts. In the case of colloidal deposition, the beneficial effect of the hydroxyl groups on the catalyst surface dominates the performance, and thus the gold on the Fe_OH is the more active system for this synthetic pathway.

4. Conclusion

In summary, we have prepared active gold-iron oxide catalysts with uniform size of ~ 2 nm for gold nanoparticles by both deposition-precipitation and colloidal-deposition methods, and further investigated the main factors in governing the catalytic activity of Au. An inverse order of catalytic

activity was found between deposition-precipitation (Au/Fe_OH < Au/Fe_O) and colloidal deposition (Au/Fe_OH > Au/Fe_O) system. Higher level of effectiveness of interaction between gold and the oxide support is suggested to account for the superiority of the oxide support (Fe_O) in the deposition-precipitation system, while surface hydroxyls induce the high reactivity of gold on the hydrated iron oxide support (Fe_OH) for the colloidal-precipitation approach. Thus, the formation mechanism of the gold species, which is directly related to the synthesis strategy, is a key factor which contributes to the activity of iron oxide supported gold catalysts, in addition to structural effects.

5. Author Information

Corresponding Author

jiacj@sdu.edu.cn; sirui@sinap.ac.cn

Notes

The authors declare no competing financial interest.

6. Acknowledgments

Financial supported from the National Science Foundation of China (NSFC) (grant nos. 21301107, 21373259 and 11079005), Fundamental research funding of Shandong University (grant nos. 2014JC005), the Taishan Scholar project of Shandong Province (China), and the Hundred Talents project of the Chinese Academy of Sciences, the Strategic Priority Research Program of the Chinese Academy of Sciences (grant no. XDA09030102), the Alexander von Humboldt Foundation and the Max-Planck Society are greatly acknowledged. The work done at Brookhaven National Laboratory was

supported by the DOE BES, by the Materials Sciences and Engineering Division under contract DE-AC02-98CH10886, and through the use of the Center for Functional Nanomaterials.

7. References

[1] M. Haruta, S. Tsubota, T. Kobayashi, H. Kageyama, M.J. Genet, B. Delmon, J. Catal. 144 (1993) 175–192.

[2] G.C. Bond, D.T. Thompson, Gold Bull. 33 (2000) 41–50.

[3] A.S.K. Hashmi, G.J. Hutchings, Angew. Chem. Int. Ed. 45 (2006) 7896–7936.

[4] A.A. Herzing, C.J. Kiely, A.F. Carley, P. Landon, G.J. Hutchings, Science 321 (2008) 1331–1335.

[5] Y. Liu, C.-J. Jia, J. Yamasaki, O. Terasaki, F. Schuth, Angew. Chem. Int. Ed. 49 (2010) 5771–5775.

[6] J. Guzman, B.C. Gate, J. Am. Chem. Soc. 126 (2004) 2672–2673.

[7] G.J. Hutchings, M.S. Hall, A.F. Carley, P. Landon, B.E. Solsona, C.J. Kiely, A. Herzing, M. Makkee, J.A. Moulijn, A. Overweg, J.C. Fierro-Gonzalez, J. Guzman, B.C. Gates, J. Catal. 242 (2006) 71–81.

[8] N. Weiher, E. Bus, L. Delannoy, C. Louis, D.E. Ramaker, J.T. Miller, J.A. van Bokhoven, J. Catal. 240 (2006) 100–107.

[9] M.M. Schubert, S. Hackenberg, A.C. van Veen, M. Muhler, V. Plzak, R.J. Behm, J. Catal. 197 (2001) 113–122.

[10] M. Kotobuki, R. Leppelt, D.A. Hansgen, D. Widmann, R.J. Behm, J. Catal. 264 (2009) 67–76.

[11] S. Carrettin, P. Concepción, A. Corma, J.M. Lopez Nieto, V.F. Puntes, Angew. Chem. Int. Ed 43 (2004) 2538–2540.

[12] S. Carrettin, Y. Hao, V. Aguilar-Guerrero, B. C. Gates, S. Trasobares, J. J. Calvino, A. Corma, *Chem. Eur. J.* **2007**, 13, 7771–7779.

[13] M. Comotti, W.C. Li, B. Spliethoff, F. Schuth, J. Am. Chem. Soc. 128 (2006) 917–924.

[14] C.-J. Jia, Y. Liu, H. Bongard, F. Schuth, J. Am. Chem. Soc. 132 (2010) 1520–1522.

[15] XY. Liu, M.H. Liu, Y.C. Luo, C.Y. Mou, S.D. Lin, H. Cheng, J.M. Chen, J.F. Lee, T.S. Lin, J. Am. Chem. Soc. 134 (2012) 10251–10258.

[16] N. Ta, J.Y. Liu, S. Chenna, P.A. Crazier, Y. Li, A.L. Chen, W.J. Shen, J. Am. Chem. Soc. 134 (2012) 20585–20588.

[17] L. Li, A.Q. Wang, B.T. Qiao, J. Lin, Y.Q. Huang,; X.D. Wang, T. Zhang, J. Catal. 229 (2013) 90–100.

[18] R. Zanella, S. Giorgio, C. Shin, C.R., Henry, C. Louis, J. Catal. 222 (2004) 357–367.

[19] X. Wang, J.A. Rodriguez, J.C. Hanson, M. Pérez, J. Evans, J. Chem. Phys. 123 (2005) 221101.

[20] W. Deng, A.I. Frenkel, R. Si, M. Flytzani-Stephanopoulos, J. Phys. Chem. C 112 (2008) 12834–12840.

[21] L.F. Allard, A. Borisevich, W. Deng, R. Si, M. Flytzani-Stephanopoulos, Overbury, S.H. J. Electron Micro. 58 (2009) 199–212.

[22] M.T. Bore, H.N. Pham, E.E. Switzer, T.L. Ward, A. Fukuoka, A.K. Datye, J. Phys. Chem. B 109 (2005) 2873–2880.

[23] M. Date, M. Haruta, J. Catal. 201 (2001) 221–224.

[24] G.M. Veith, A.R. Lupini, S.J. Pennycook, N.J. Dudney, ChemCatChem 2 (2010) 281–286.

[25] J.A. Singh, S.H. Overbury, N.J. Dudney, M.J. Li, G.M. Veith, ACS Catal. 2 (2012) 1138–1146.

[26] J. Lin, B.T. Qiao, L. Lin, H.L. Guan, C.Y. Ruan, A.Q. Wang, W.S. Zhang, X.D. Wang, T. Zhang, J. Catal. 319 (2014) 142–149.

[27] W. Deng, C. Carpenter, N. Yi, M. Flytzani-Stephanopoulos, Top. Catal. 44 (2007) 199–208.

[28] A. Piovano, G. Agostini, A.I. Frenkel, T. Bertier, C. Prestipino, M. Ceretti, W. Paulus, C. Lamberti, J. Phys. Chem. C 115 (2011) 1311–1322.

Table 1 Characterization of gold catalyst.

Sample	Au (wt.%) [a]	Phase [b]	D (nm) [c]	S ($m^2 \cdot g^{-1}$) [d]
DP_Au/Fe_OH	0.92	Amorphous	2.2±0.6	210
DP_Au/Fe_O	0.89	α-Fe_2O_3	2.0±0.5	69
CD_Au/Fe_OH	0.98	Amorphous	2.0±0.6	210
CD_Au/Fe_O	0.96	α-Fe_2O_3	2.1±0.6	66

[a] Determined by ICP-AES;

[b] Identified from XRD patterns for calcined catalysts;

[c] Mean Au particle sizes of calcined catalysts, which were calculated from > 100 nanoparticles in HRTEM images;

[d] BET surface areas for calcined catalysts;

Table 2 EXAFS fitting results (*R*: distance; CN: coordination number) of gold catalysts.

Sample	Au-O		Au-Au	
	R (Å)	CN	*R* (Å)	CN
Au foil	—	—	2.86±0.00	12
DP_Au/Fe_OH (dried)	2.00±0.02	2.5±0.4	—	—
DP_Au/Fe_O (dried)	2.00±0.00	2.9±0.2	—	—
CD_Au/Fe_OH (dried)	—	—	2.84±0.01	11.1±1.4
CD_Au/Fe_O (dried)	—	—	2.83±0.01	10.4±2.2
DP_Au/Fe_OH (calcined)	—	—	2.84±0.02	9.9±2.1
DP_Au/Fe_O (calcined)	—	—	2.84±0.01	9.8±1.5
DP_Au/Fe_OH (used)	—	—	2.87±0.01	10.1±1.6
DP_Au/Fe_O (used)	—	—	2.84±0.01	10.5±1.5

Table 3 Hydrogen consumption (*H_2-consump.*) of gold catalysts.

Sample	Reduction peak (°C)	Experimental *H_2-consump.* ($\mu mol \cdot g^{-1}$)	Theoretical *H_2-consump.* ($\mu mol \cdot g^{-1}$) [a]
DP_Au/Fe_OH	128	437	1300
DP_Au/Fe_O	67, 232	1444	1510
CD_Au/Fe_OH	188, 340	235	1300
CD_Au/Fe_O	257	1042	1510

[a] Calculated according to Fe_OH→Fe_3O_4 or Fe_2O_3→Fe_3O_4.

Figure Captions:

Scheme 1 Schematic demonstration of the formation pathways of the different Au/FeO_x catalysts.

Figure 1 XRD patterns of calcined Au/FeO_x samples: (a) DP_Au/Fe_OH; (b) CD_Au/Fe_OH; (c) DP_Au/Fe_O; (d) CD_Au/Fe_O.

Figure 2 TEM/HRTEM and HAADF-STEM images of (a) dried DP_Au/Fe_OH; (b) dried DP_Au/Fe_O; (c) calcined DP_Au/Fe_OH; (d) calcined DP_Au/Fe_O; (e) used DP_Au/Fe_OH; (f) used DP_Au/Fe_O.

Figure 3 TEM/HRTEM images of (a) dried CD_Au/Fe_OH; (b) dried CD_Au/Fe_O; (c) calcined CD_Au/Fe_OH; (d) calcined CD_Au/Fe_O; (e) used CD_Au/Fe_OH; (f) used CD_Au/Fe_O.

Figure 4 XANES profiles (a,b) and EXAFS R space fittings (c,d) of Au/FeO_x samples: (a,c) DP_Au/Fe_OH; (b,d) DP_Au/Fe_O.

Figure 5 XANES profiles (a) and EXAFS R space spectra (b) of Au/FeO_x samples (CD_Au/Fe_OH and CD_Au/Fe_O).

Figure 6 CO conversions of Au/FeO_x samples measured under (a) transient conditions and (b) at a constant temperature of 30 °C (1%CO/20%O_2/79%N_2, 80,000 $mL \cdot h^{-1} \cdot g_{cat}^{-1}$).

Figure 7 CO conversions (blue) and Au oxidation states (red) of (a) DP_Au/Fe_OH and (b) DP_Au/Fe_O as function of reaction time (1%CO/16%O_2/83%He, 20 $mL \cdot min^{-1}$, 25 mg, at 25 °C). Inserts are corresponding XANES spectra taken at the start and end points.

Figure 8 H_2-TPR profiles (a) and XRD patterns (b,c) under the in-situ conditions of TPR test: (b) DP_Au/Fe_OH; (c) DP_Au/Fe_O.

Figure 9 H_2-TPR profiles (a) and XRD patterns (b,c) under the in-situ conditions of TPR test: (b) CD_Au/Fe_OH; (c) CD_Au/Fe_O.

Scheme 1

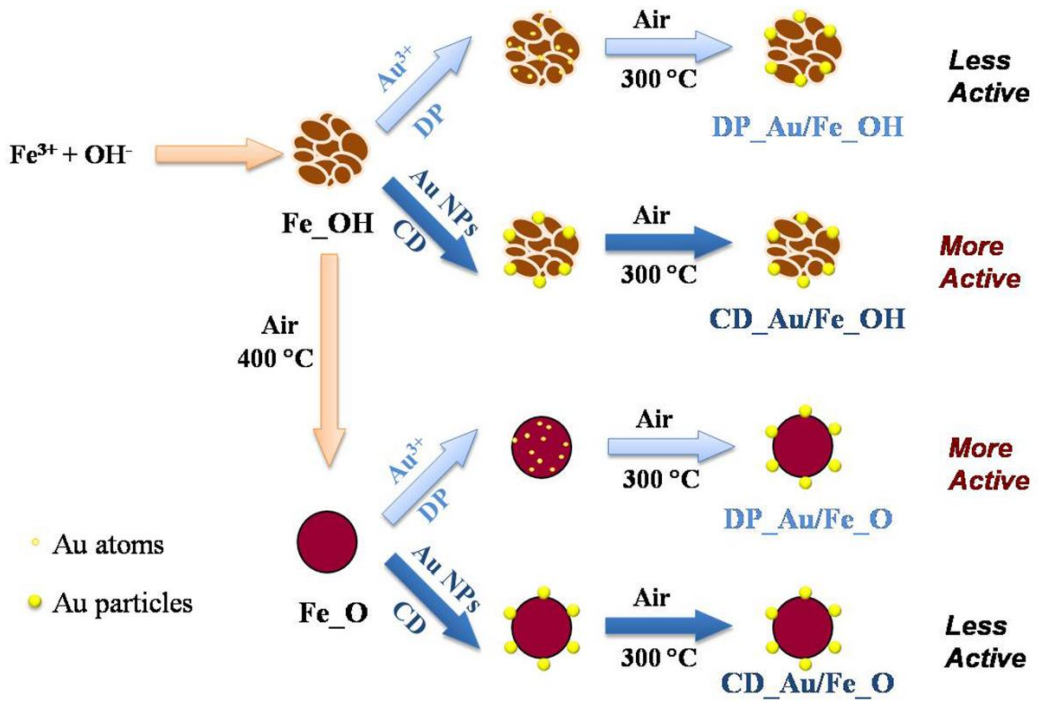

Scheme 1 Schematic demonstration of the formation pathways of the different Au/FeO_x catalysts.

Figure 1

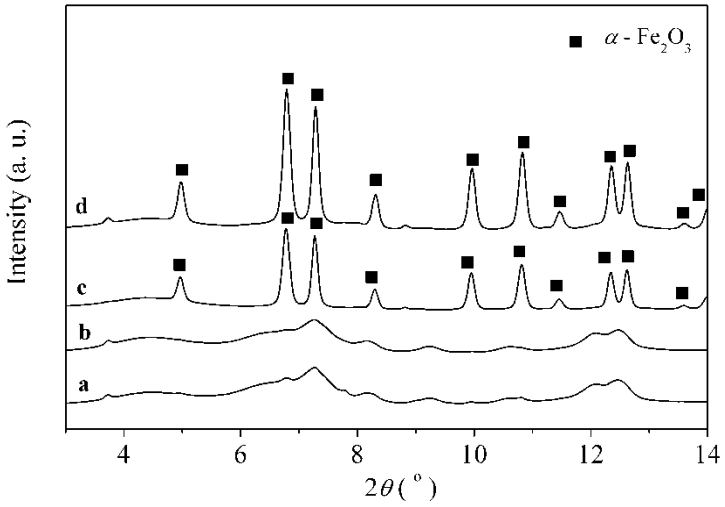

Figure 1 XRD patterns of calcined Au/FeO_x samples: (a) DP_Au/Fe_OH; (b) CD_Au/Fe_OH; (c) DP_Au/Fe_O; (d) CD_Au/Fe_O.

Figure 2

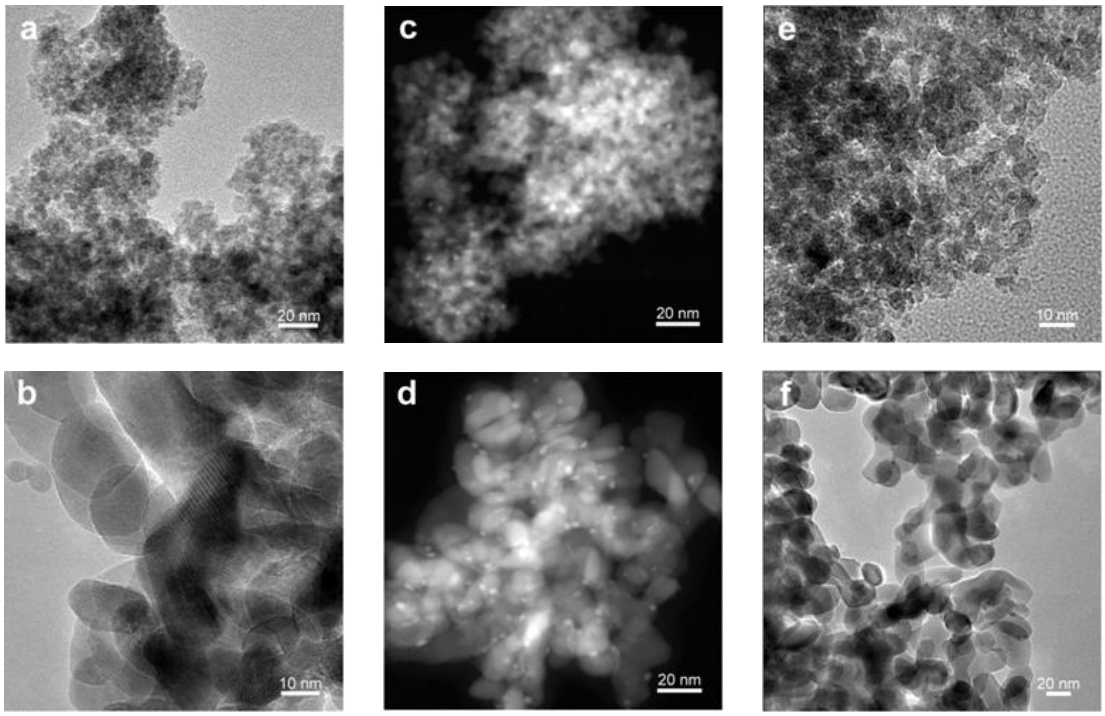

Figure 2 TEM/HRTEM and HAADF-STEM images of (a) dried DP_Au/Fe_OH; (b) dried DP_Au/Fe_O; (c) calcined DP_Au/Fe_OH; (d) calcined DP_Au/Fe_O; (e) used DP_Au/Fe_OH; (f) used DP_Au/Fe_O.

Figure 3

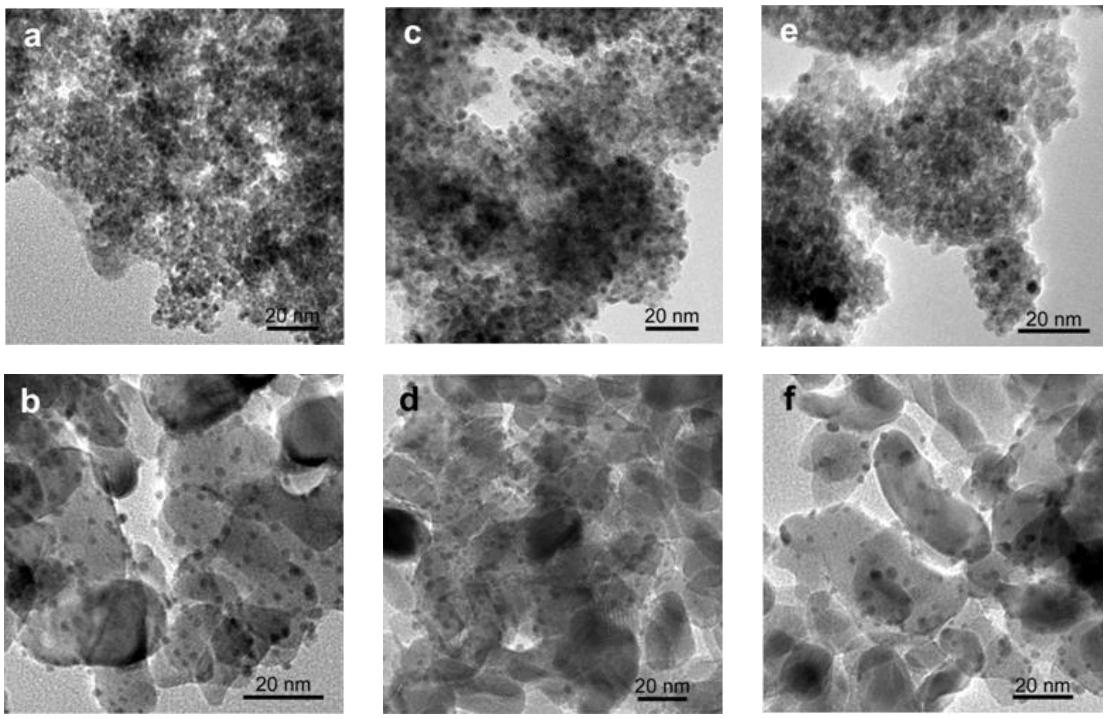

Figure 3 TEM/HRTEM images of (a) dried CD_Au/Fe_OH; (b) dried CD_Au/Fe_O; (c) calcined CD_Au/Fe_OH; (d) calcined CD_Au/Fe_O; (e) used CD_Au/Fe_OH; (f) used CD_Au/Fe_O.

Figure 4

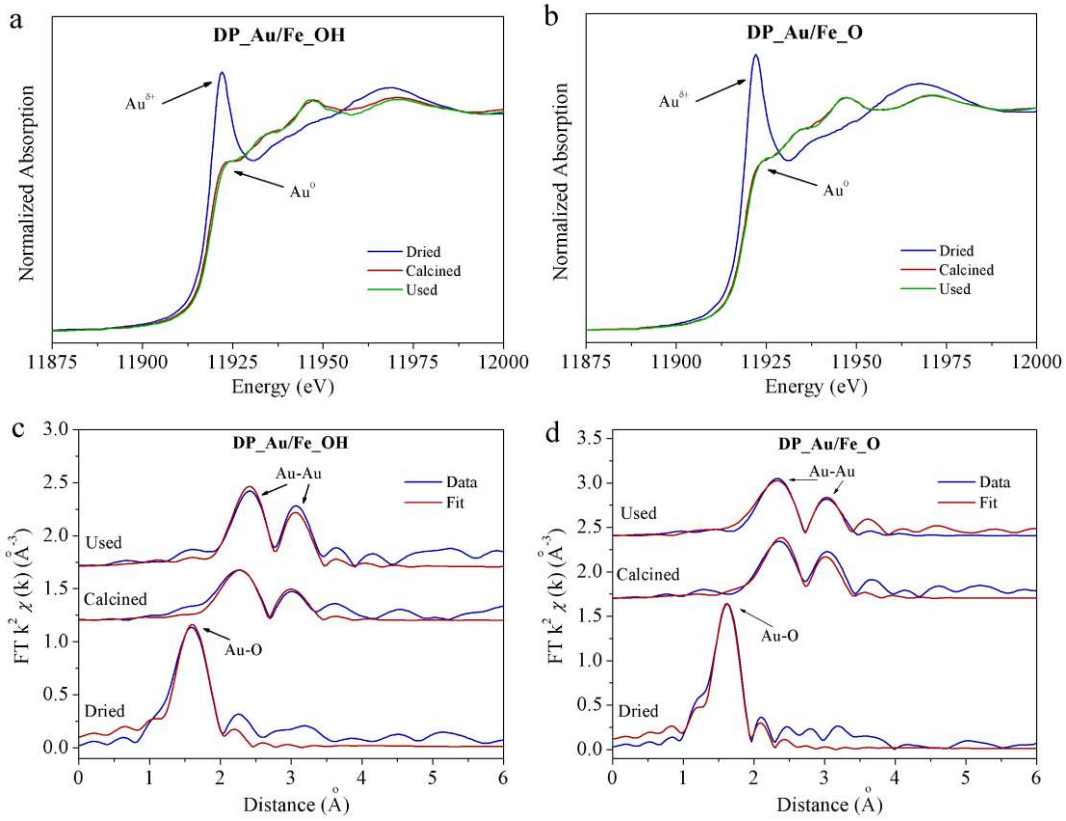

Figure 4 XANES profiles (a,b) and EXAFS R space fittings (c,d) of Au/FeO_x samples: (a,c) DP_Au/Fe_OH; (b,d) DP_Au/Fe_O.

Figure 5

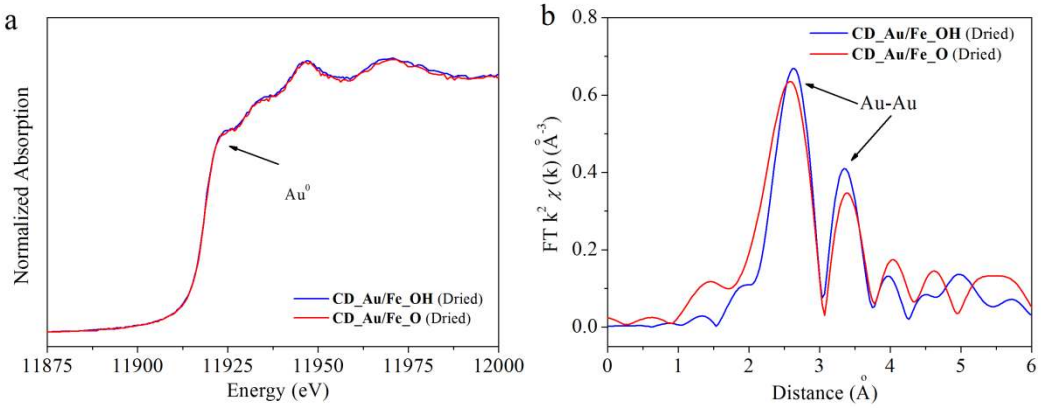

Figure 5 XANES profiles (a) and EXAFS R space spectra (b) of Au/FeO_x samples (CD_Au/Fe_OH and CD_Au/Fe_O).

Figure 6

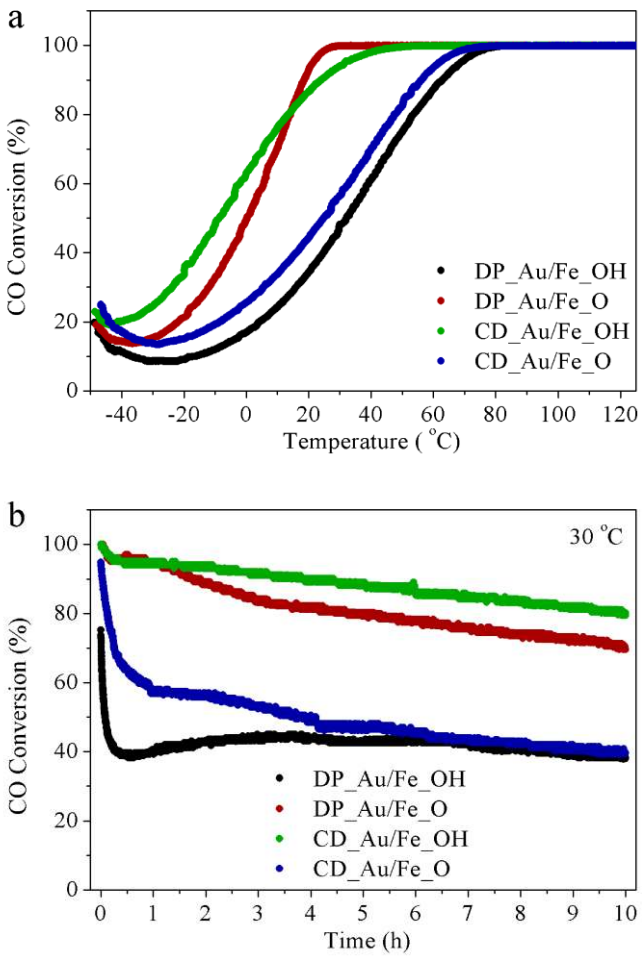

Figure 6 CO conversions of Au/FeO_x samples measured under (a) transient conditions and (b) at a constant temperature of 30 °C (1%CO/20%O_2/79%N_2, 80,000 $mL \cdot h^{-1} \cdot g_{cat}^{-1}$).

Figure 7

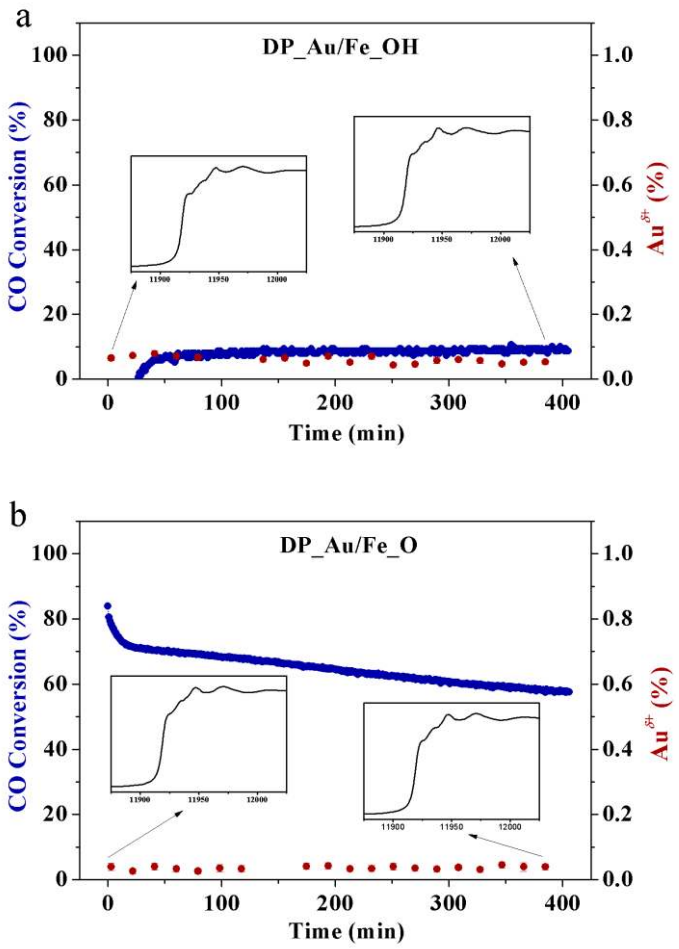

Figure 7 CO conversions (blue) and Au oxidation states (red) of (a) DP_Au/Fe_OH and (b) DP_Au/Fe_O as function of reaction time (1%CO/16%O_2/83%He, 20 mL·min^{-1}, 25 mg, at 25 °C). Inserts are corresponding XANES spectra taken at the start and end points.

Figure 8

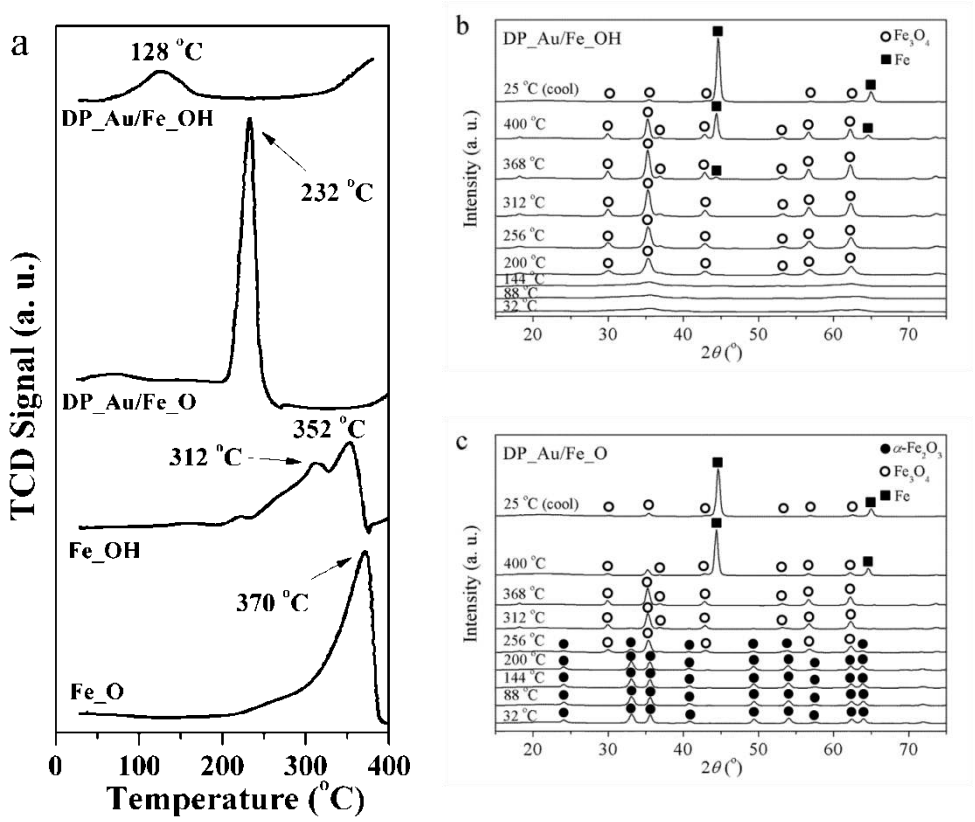

Figure 8 H_2-TPR profiles (a) and XRD patterns (b,c) under the in-situ conditions of TPR test: (b) DP_Au/Fe_OH; (c) DP_Au/Fe_O.

Figure 9

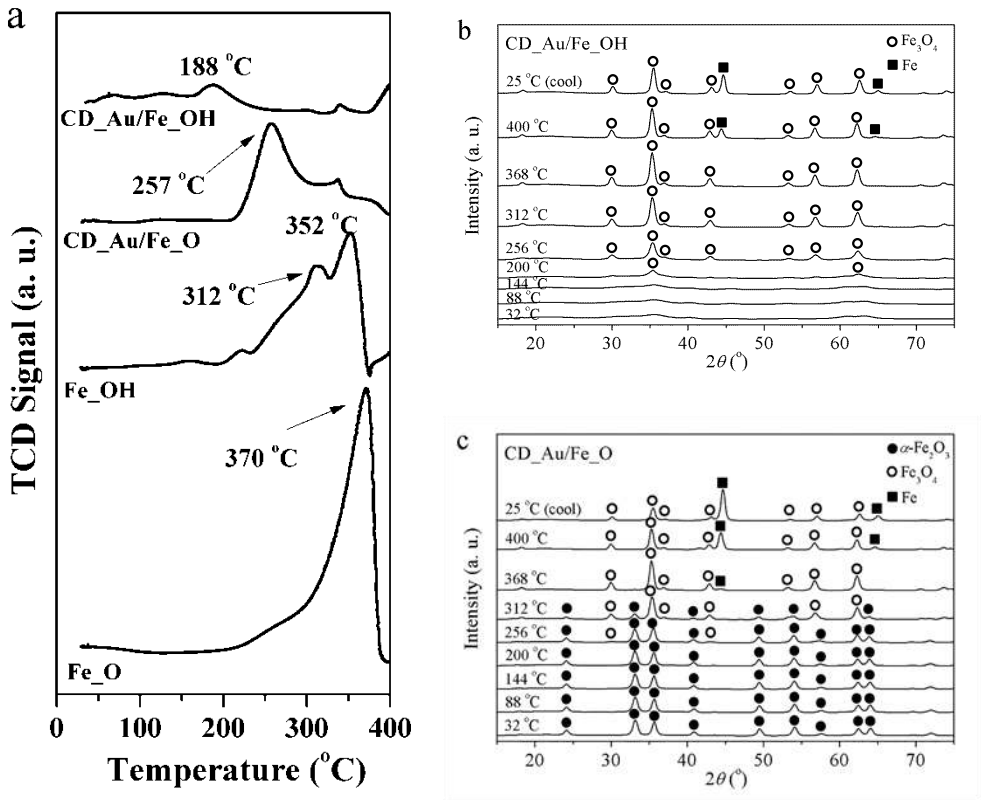

Figure 9 H_2-TPR profiles (a) and XRD patterns (b,c) under the in-situ conditions of TPR test: (b) CD_Au/Fe_OH; (c) CD_Au/Fe_O.